

Aerodynamic actuation characteristics of radio-frequency discharge plasma and control of supersonic flow

Zhen Yang(杨臻), Hui-Min Song(宋慧敏), Hong-Yu Wang(王宏宇), Shan-Guang Guo(郭善广), Min Jia(贾敏), Kang Wang(王康)

Citation: Chin. Phys. B . 2019, 28(2): 024701. **doi:** 10.1088/1674-1056/28/2/024701
Journal homepage: http://cpb.iphy.ac.cn; http://iopscience.iop.org/cpb

What follows is a list of articles you may be interested in

UAV flight test of plasma slats and ailerons with microsecond dielectric barrier discharge

Zhi Su(苏志), Jun Li(李军), Hua Liang(梁华), Bo-Rui Zheng(郑博睿), Biao Wei(魏彪), Jie Chen(陈杰), Li-Ke Xie(谢理科)
Chin. Phys. B . 2018, 27(10): 105205. **doi:** 10.1088/1674-1056/27/10/105205

Mechanism of controlling turbulent channel flow with the effect of spanwise Lorentz force distribution

Yang Han(韩洋), Hui Zhang(张辉), Bao-Chun Fan(范宝春), Jian Li(李健), Dai-Wen Jiang(江代文), Zi-Jie Zhao(赵子杰)
Chin. Phys. B . 2017, 26(8): 084704. **doi:** 10.1088/1674-1056/26/8/084704

Comparison between AlN and Al_2O_3 ceramics applied to barrier dielectric of plasma actuator

Dong-Liang Bian(卞栋梁), Yun Wu(吴云), Min Jia(贾敏), Chang-Bai Long(龙昌柏), Sheng-Bo Jiao(焦胜博)
Chin. Phys. B . 2017, 26(8): 084703. **doi:** 10.1088/1674-1056/26/8/084703

Flow control of micro-ramps on supersonic forward-facing step flow

Qing-Hu Zhang(张庆虎), Tao Zhu(朱涛), Shihe Yi(易仕和), Anping Wu(吴岸平)
Chin. Phys. B . 2016, 25(5): 054701. **doi:** 10.1088/1674-1056/25/5/054701

Wind tunnel experiments on flow separation control of an Unmanned Air Vehicle by nanosecond discharge plasma aerodynamic actuation

Kang Chen(陈康) and Hua Liang(梁华)
Chin. Phys. B . 2016, 25(2): 024703. **doi:** 10.1088/1674-1056/25/2/024703

Aerodynamic actuation characteristics of radio-frequency discharge plasma and control of supersonic flow*

Zhen Yang(杨臻), Hui-Min Song(宋慧敏)†, Hong-Yu Wang(王宏宇), Shan-Guang Guo(郭善广), Min Jia(贾敏), and Kang Wang(王康)

Science and Technology on Plasma Dynamics Laboratory, Air Force Engineering University, Xi'an 710038, *China*

(Received 2 September 2018; revised manuscript received 10 October 2018; published online 10 January 2019)

In this paper, aerodynamic actuation characteristics of radio-frequency (RF) discharge plasma are studied and a method is proposed for shock wave control based on RF discharge. Under the static condition, a RF diffuse glow discharge can be observed; under the supersonic inflow, the plasma is blown downstream but remains continuous and stable. Time-resolved schlieren is used for flow field visualization. It is found that RF discharge not only leads to continuous energy deposition on the electrode surface but also induces a compression wave. Under the supersonic inflow condition, a weak oblique shock wave is induced by discharge. Experimental results of the shock wave control indicate that the applied actuation can disperse the bottom structure of the ramp-induced oblique shock wave, which is also observed in the extracted shock wave structure after image processing. More importantly, this control effect can be maintained steadily due to the continuous high-frequency (MHz) discharge. Finally, correlations for schlieren images and numerical simulations are employed to further explore the flow control mechanism. It is observed that the vortex in the boundary layer increases after the application of actuation, meaning that the boundary layer in the downstream of the actuation position is thickened. This is equivalent to covering a layer of low-density smooth wall around the compression corner and on the ramp surface, thereby weakening the compressibility at the compression corner. Our results demonstrate the ability of RF plasma aerodynamic actuation to control the supersonic airflow.

Keywords: radio-frequency (RF) discharge plasma, surface discharge, flow control, aerodynamic actuation

PACS: 47.40.–x, 47.40.Ki, 52.70.Gw, 52.80.Pi **DOI:** 10.1088/1674-1056/28/2/024701

1. Introduction

Plasma flow control (PFC) has become an effective method for active control mode in recent years. Previous studies have shown that plasma aerodynamic actuation can effectively improve the structure of a supersonic flow field, such as controlling boundary layer transition, reducing flow instability and sonic boom mitigation.[1–4] Shock wave control has also drawn increasing attention, mainly focusing on reducing the shock wave drag on aircraft, improving the shock wave structure of the inlet at off-designed state, achieving thrust vector control by inducing an oblique shock wave, *etc*.[5,6]

Leonov and Yarantsev employed quasi-direct-current surface arc discharge to examining discharge characteristics and supersonic flow control. Under the supersonic condition, an oblique shock wave was induced by plasma actuation, and flow parameters were greatly affected by the loading power. At the same time, the angle of oblique shock wave dropped from 60° to 45° after the application of actuation during the ramp-induced shock wave control, and the surface resistance in downstream of the actuation position also decreased significantly.[7] Menier *et al.* carried out the experiments on controlling the supersonic flow field by direct current (DC) discharge plasma aerodynamic actuation and concluded that pressure distribution on the plate surface and shock wave angle are dependent on the polarity of the electrode. Hence, it can be inferred that the action mechanism of plasma actuation included both the heating effect and kinetic momentum of the charges.[8] Joussot *et al.* analyzed the control mechanism and established that the effect of heating wire on the oblique shock wave was about half of that under plasma actuation. This also indicates that ionization effect of plasma plays an important role in flow control.[9] Jin *et al.* explored the evolution of plasma synthetic jet under static condition by means of time-resolved schlieren photography and found that the jet velocity can reach up to 100 m/s. After applying the actuation an oblique shock wave can be induced under supersonic inflow with a Mach number of 2.[10] Nishihara *et al.* focused on the control of cylinder-detached shock wave by using ns-DBD plasma actuator, which is installed on the surface of cylinder. Using a supersonic inflow at a Mach number of 5, the detached distance of the detached shock wave under plasma actuation was enhanced by 25%, which corresponds to the shock wave weakening.[11,12] Lashkov *et al.* showed that detached shock wave can be controlled by microwave discharge plasma. Both schlieren images and pressure measurements demonstrated that the actuation led the shock wave to move upstream, the detached distance to increase, and the intensity to weaken.[13] Wang *et al.* investigated the instabil-

*Project supported by the National Natural Science Foundation of China (Grant Nos. 11472306, 51407197, and 51507187).

†Corresponding author. E-mail: min_cargi@sina.com

© 2019 Chinese Physical Society and IOP Publishing Ltd

ity of shock wave/boundary layer by using array synthetic jet discharge. Multiple discharging circuits were arranged for increasing spanwise disturbance. Under the application of actuation, the separation zone of shock wave decreased in size and the separated and reattached shock waves moved upstream.[14]

Based on the discharge mode, the plasma aerodynamic actuation can be classified as arc discharge actuation, dielectric barrier discharge actuation, plasma synthetic jet actuation, *etc*.; based on the discharge power frequency, it can be classified as direct discharge, ns-pulsed discharge, radio-frequency (RF) discharge actuation and microwave discharge actuation, *etc*. Compared with other discharge styles, RF discharge exhibits several advantages including high heating efficiency, strong discharge stability, and convenient power adjustment.[15,16] In particular, previous studies also confirmed the favorable thermal effect of RF-DBD.[17] All of these suggest that RF plasma has great potential in shock wave control. However, due to shortcomings such as unfocused discharge energy and low induced velocity for DBD, the shock wave control effect by RF DBD is very weak, which has been confirmed in previous studies.[18] Hence, to overcome these limitations, RF surface discharge actuator is proposed for its potential in higher concentrated discharge energy. Furthermore, RF surface discharge may impose a persistent disturbance on shock wave due to the high-frequency sine voltage waveform, which means that its discharge stability may be better than the pulse surface discharge stability. In this study, the aerodynamic actuation characteristics of RF surface discharge plasma are first investigated, including the discharge and flow field characteristics. Then, the experimental investigations of induction of shock wave and ramp-induced oblique shock wave control by aerodynamic actuation are performed. Finally, the control mechanism is analyzed from correlations and numerical simulations, along with the acquisition of flow field parameters such as density and wall pressure before and after the actuation.

2. Experimental system

2.1. Supersonic wind tunnel

Figure 1 shows the structure of a supersonic wind tunnel with a Mach number of 2, which mainly consists of rectification, supersonic nozzle, test section, diffuser and vacuum pump. Prior to starting the experiment, the tunnel is set up until working pressure decreases to 5 kPa. When the tunnel is started, the polyethylene(PE) film fixed on the nozzle exit is broken down and stable operation of the wind tunnel can be maintained for 2 s–3 s. Multiple shielding nets are arranged in the rectification to ensure uniform distribution of airflow in the test section. The specimen is placed in the test section. Images of discharging process and flow field are acquired through the vertical and horizontal optical inspection windows. Table 1 shows the detailed flow conditions of the wind tunnel. The total pressure of the incoming flow in the wind tunnel is P_0, the total temperature is T_0, P_S and T_S are the static pressure and static temperature, respectively, the unit Reynolds number of the wind tunnel is Re^{-1}, ρ and u_∞ are the density and velocity of incoming flow, respectively.

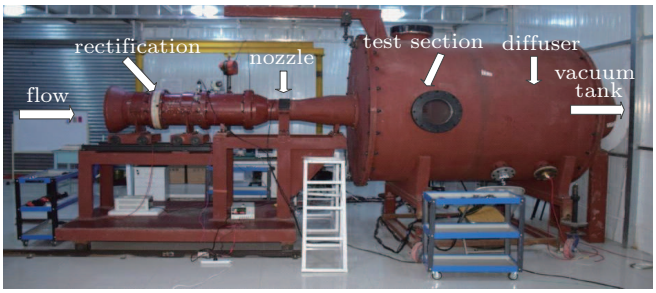


Fig. 1. Supersonic wind tunnel with Mach number of 2.

Table 1. Detailed flow conditions of wind tunnel.

Parameters	P/kPa	T/K	P_s/kPa	T_s/K	Ma	ρ/(kg/m^3)	U_∞/(m/s)	Re^{-1}
Value	95.6	296	12.218	164.4	2	0.259	514.1	1.19×10^7

2.2. Circuit system

As shown in Fig. 2, the discharge circuit is mainly composed of an RF power supply, impedance matching circuit, plasma actuator and discharge diagnostic systems. The RF power supply (AG 1071L, T & C) operates in a frequency range of 10 kHz–10 MHz, and the maximum power in continuous operation can reach up to 500 W. The impedance matching circuit is designed to add as much as load power into the actuator as possible, and is connected between the RF power supply and the surface discharge actuator. The discharge voltage and current waveform are measured with a high-voltage probe and current probe. The voltage probe used in this paper is Tektronix P6015 A with an attenuation ratio of 1:00, which can test dc 20 kV and pulse 40-kV voltage. The current probe is Tektronix TCP0030A with 120-MHz bandwidth, which has a wide range of test. The test signal is displayed and recorded by Tektronix DPO4104 digital oscilloscope. This oscilloscope has four acquisition channels with sampling frequency up to 5 GHz/s, and has the function of an output trigger signal, which can fully meet the requirements for the experiment.

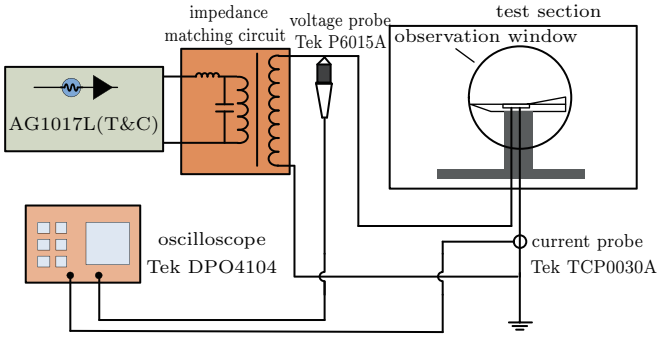


Fig. 2. Schematic diagram of circuit system.

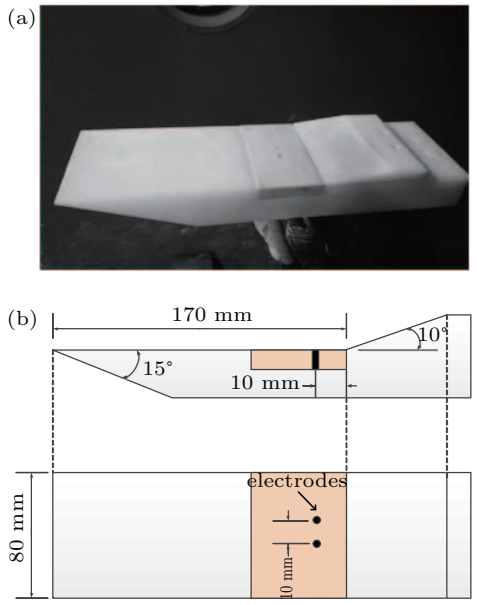


Fig. 3. (a) Plate-ramp experimental specimen, and (b) physical model.

As shown in Fig. 3, the discharge actuator is installed in the groove on the surface of plate-ramp experimental specimen. The surface discharge actuator consists of a ceramic dielectric flat plate and two tungsten electrodes each with a diameter of 2 mm, which are arranged in a spanwise pattern. The electrodes are vertically embedded in the dielectric plate with spacing of 10 mm, and it is installed 10 mm away from the front edge of the ramp. The width of the flat plate is 80 mm and the inclination angle of wedge-shape part in the front is 15°. The distance between the leading edge of the plate and the compression corner of the ramp is 170 mm, and the inclination angle of the ramp is 10°. In order to minimize the experimental error the surface of the actuator and plate are subject to mirror polishing.

2.3. Schlieren system and synchronization system

In this study, a schlieren system with typical Z-shaped structure is used to observe the flow field. The system consists of a white xenon light source, two concave mirrors each with a focal length of 300 mm, a vertical knife edge, and a high-speed camera (Phantom V2511). The sampling rate of the high-speed camera is set to be 4×10^4 Hz, the exposure time is set to be 1 μs, and the pixel array is 1280×400.

Figure 4 shows the synchronization system, which was included a wind tunnel, high-speed camera and power supply. The pressure signal from the starting of the wind tunnel is used for triggering the oscilloscope. Because the supersonic wind tunnel in the laboratory needs about 0.2 s to stabilize the flow field after starting up, the time delay is set to be 0.5 s to ensure that the power supply is triggered for discharging after the generation of a stable flow field. Accordingly, both the reference flow field and the flow field after the application of actuation are captured by the high-speed camera.

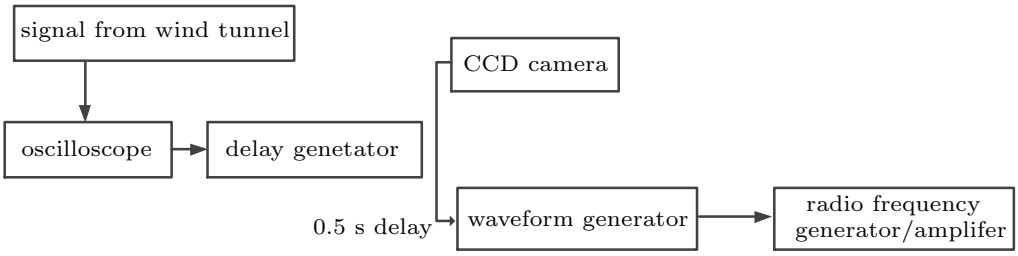


Fig. 4. Schematic diagram of synchronization system.

3. RF discharge plasma aerodynamic actuation characteristics

3.1. Discharge characteristics under RF discharge plasma aerodynamic actuation

Figures 5(a) and 5(b) show the waveforms and images acquired during RF surface discharge under the static and supersonic conditions, respectively, and Table 2 presents the detailed experimental conditions. From the voltage and current waveform, it can be concluded that the peak current drops from 2.2 A to 1.8 A, whereas peak voltage increases from 2350 V to 2600 V under the supersonic airflow. This trend is similar to the scenario of RF-DBD discharge.[18] From the surface DC discharge theory,[7] it can be inferred that charged particles around the electrode are blown away by supersonic airflow, leading to a drop in the concentration of charged particles and a subsequent decline in discharge current. The increase in the voltage peak can be explained by the fact that a greater breakdown voltage is required under lower particle concentration according to the theory of reduced electric field E/N.

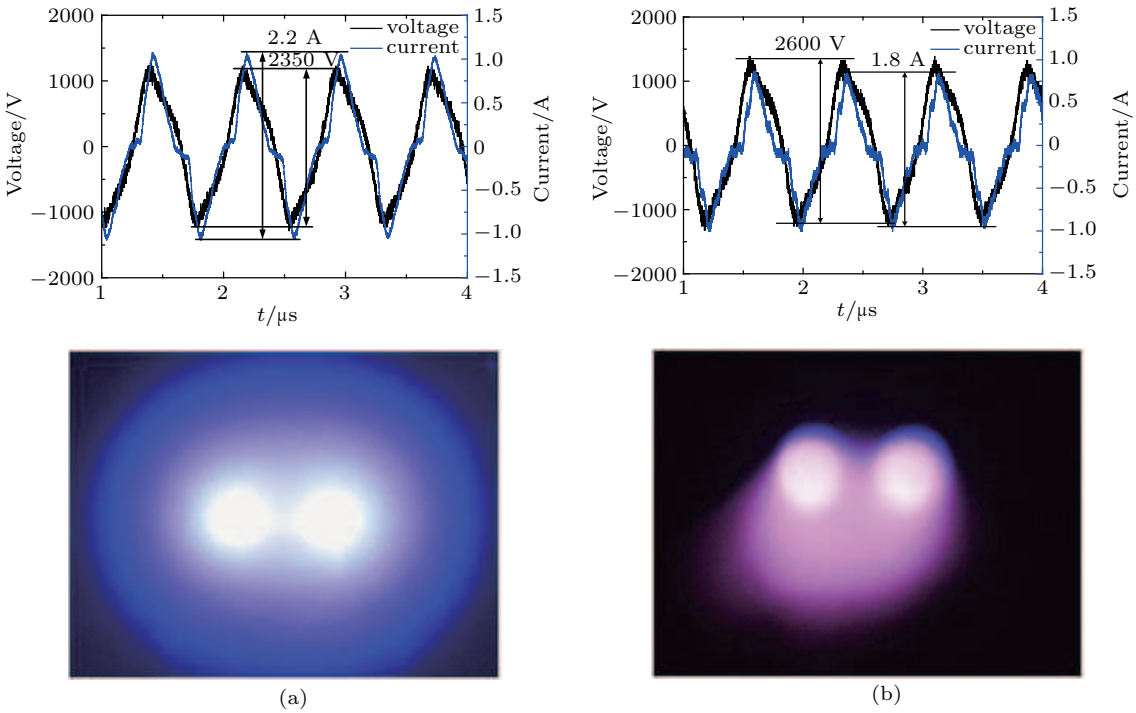


Fig. 5. Voltage–current waveforms and discharge image in (a) quiescent air and (b) supersonic airflow

Table 2. Experimental conditions. The unit 1 Torr = 1.33322×10^2 Pa.

Parameters	Output power/W	reflective power/W	Frequency/MHz	Operating pressure/Torr	*Ma*
Value	150	90	1.30	100	2

Under the static condition, the discharge mode is referred to as a diffuse glow discharge. The plasma on the electrode surface is white in color while the surrounding is violet blue. In contrast, under the supersonic condition the plasma is blown downstream and turned pink. Earlier studies showed that the surface discharge mode is mainly determined by operating pressure and power.[19] Obviously, the operating pressure on the surface of electrode is different in the case with incoming flow from that in the case without incoming flow and the gas flow also has an influence on the density of the charged particles. These factors may result in different discharge modes and colors.

3.2. Flow field characteristics under RF surface discharge plasma aerodynamic actuation

Surface discharge plasma imposes disturbance on the supersonic flow field by generating compression waves and energy deposition in the rapid heating process.[19,20] Therefore, it can be inferred that similar actuation characteristics may exist in the RF surface discharge process. In this study, the generation and propagation of RF discharge plasma are recorded by using the time-resolved schlieren technique and the effect of operating pressure (20 Torr∼ 100 Torr) on flow field characteristics is investigated. From the schlieren images, it can be observed that the RF discharge can indeed cause energy deposition on the electrode surface and induce a compression wave as shown in Fig. 6. Under the same operating pressure, the compression wave uniformly spreads all around in the air and the boundary of compression wave becomes gradually blurry, suggesting the gradually weakening intensity. At the same time, the compression wave becomes more obvious under higher operating pressure as a result of greater air density. The velocity of the compression wave changes under different operating pressures, suggesting that the intensity is not constant.

The compression wave can only be generated when triggered by the power supply; *i.e.*, no compression wave is generated in the following continuous discharge cycles. If the compression wave can be generated in each discharge cycle, then its time interval should be one period, namely about 1 μs. However, in Fig. 6, it cannot be found that new compression wave is generated during the compression wave propagation. This confirms our previous conclusion. As for the reason, in our opinion, because time delays the temperature of the electrodes and the air around both increase, this leads the pressure difference between them to decrease. In this case, it is more difficult to produce a compression wave.

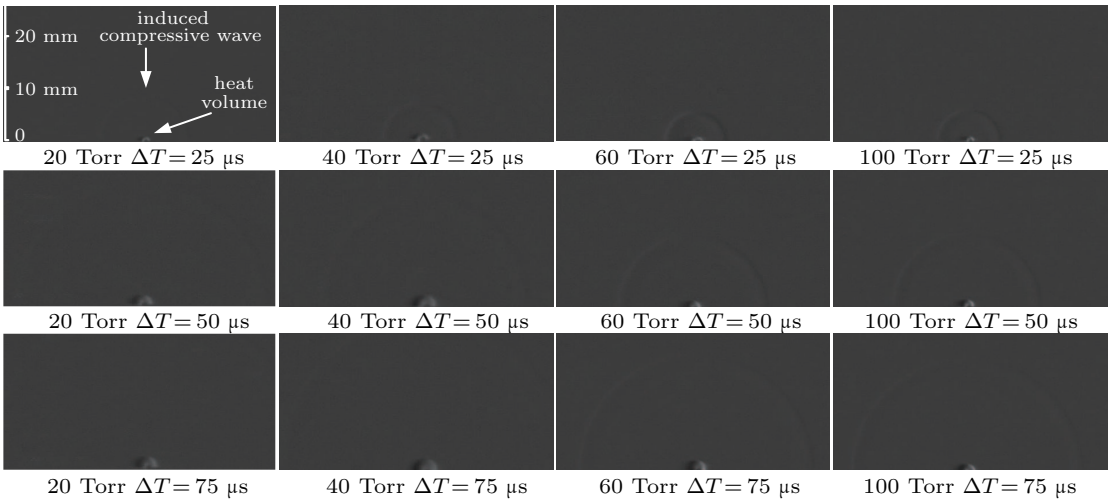


Fig. 6. Generations and propagations of RF discharge plasma under different operating pressures (20 Torr–100 Torr).

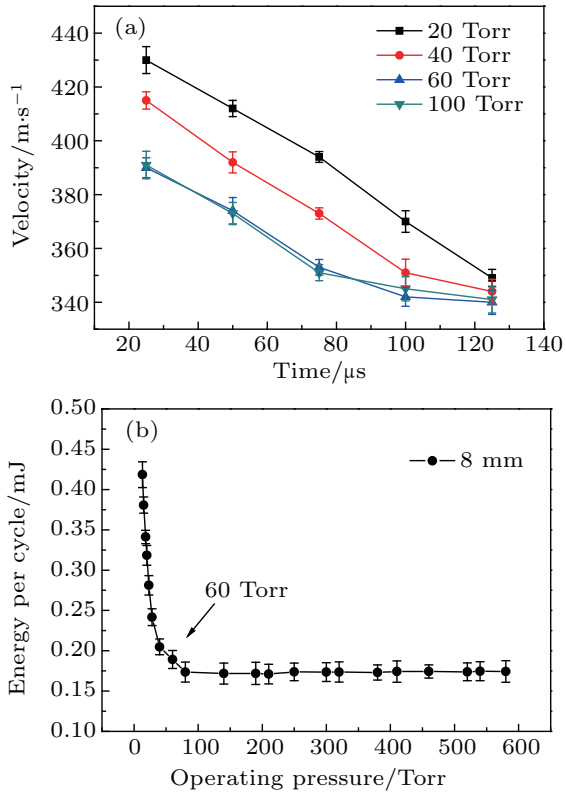


Fig. 7. (a) Variations of compression wave velocity with time at different operating pressure, and (b) variations of RF surface discharge single-cycle energy with operating pressure.

Figure 7(a) shows the variations of compression wave velocity with time under different operating pressures. Overall, the velocity of compression wave gradually decreases from its initial value to approximately 345 m/s in the propagation process. At $\Delta T = 25$ μs, the velocity of compression wave under an operating pressure of 20 Torr reaches a maximum value of 430 m/s, while the compression wave velocities under 60 Torr and 100 Torr are lowest. A previous study has concluded that the compression wave velocity is closely related to the instantaneous discharge power (single-cycle energy).[21] In Fig. 7(b) the variation of RF surface discharge single-cycle energy with operating pressure is given in the early study.[22] Combined with the rule above, the relationship between the compression wave velocity and the operating pressure can be explained as follows. At the operating pressure below 60 Torr, single-cycle energy drops gradually with the increase of operating pressure according to the charge–voltage (Q–V) Lissajous figure; therefore, it results in the same trend for the compression wave velocity, as shown in Fig. 7(a). At an operating pressure above 60 Torr, discharge mode changes from diffuse glow discharge to constricted discharge, single-cycle energy almost remains unchanged, which leads to the same trend of compression wave velocity as displayed in the figure.

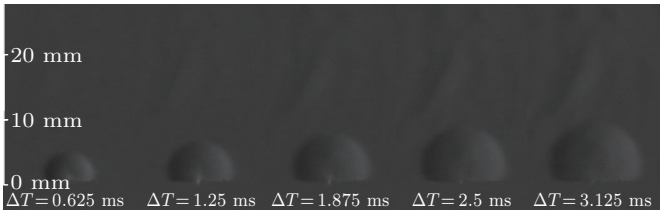


Fig. 8. Evolution of discharge energy deposition with time at 100 Torr.

Due to the continuous discharge characteristics, it is necessary to further investigate the process of discharge energy deposition. Figure 8 shows the evolution of discharge energy deposition with time at 100 Torr. As the discharge time increases, the volume of energy deposition induced by RF surface discharge increases constantly, following a semicircular cross-section. Figure 9 shows the surface temperature distribution measured by a thermal infrared imager, where the maximum discharge temperature can reach up to 570 K, which is indicative of a thermal effect. Accordingly, under supersonic inflow, continuous discharge can impose disturbance on the flow field continuously, and thus exhibits the potential for stable control.

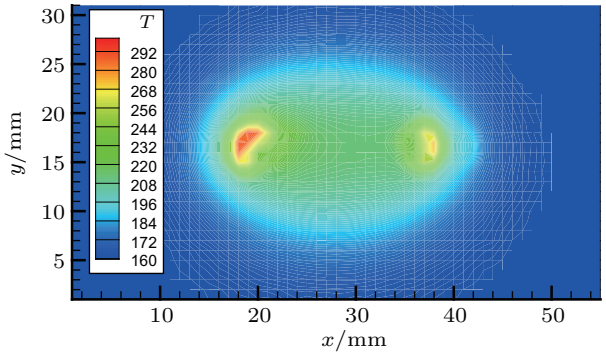


Fig. 9. Spatial distribution of surface temperature at 100 Torr.

4. Flow control by RF surface discharge aerodynamic actuation

4.1. Experiments on induction of shock wave by RF discharge plasma under supersonic condition

Although the RF discharge can induce the weak compression wave and heat air that flows through the electrode surface, it is still unclear that whether it can disturb the flow field and how it is achieved. Next, the relevant experiments on the induction of shock wave for detailed analysis are performed.

Figure 10 shows the disturbing supersonic inflow by RF discharge, and figures 10(a) and 10(b) indicate the flow field without and with actuation, respectively. After applying the actuation, it can be observed that an oblique shock wave appears around the electrodes. Therefore, the plasma can be treated as a virtual profile.[7] Furthermore, the induced oblique shock wave is stable and can be observed at the subsequent time intervals, which may be inferred to be the caused by the high-frequency continuous discharge, based on the evolution of the discharge energy deposition that is shown in Fig. 8.

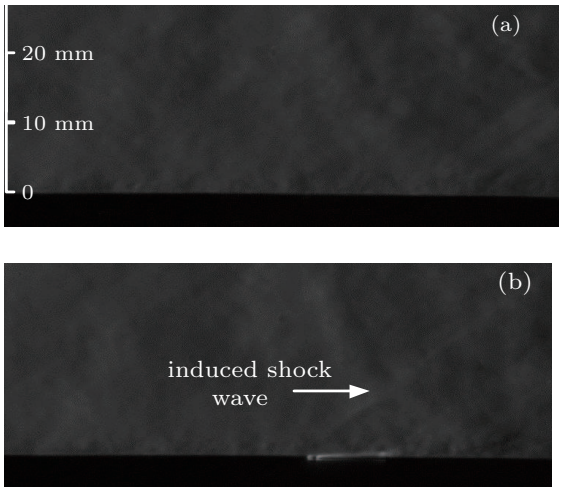


Fig. 10. Time-resolved schlieren visualization of the disturbing supersonic inflow (a) without and (b) with actuation.

To further investigate the control rules of the induction of shock wave by RF discharge plasma, the relationship between RF discharge plasma and the mainstream is determined as shown in Fig. 11. Furthermore, the angle of discharge-induced shock wave mainly relates to discharge power and the Mach number of mainstream and can be expressed as follows:[23]

$$\tan^2(\theta) = \left(\frac{\partial y}{\partial x}\right)^2 = \frac{\gamma-1}{\gamma}\frac{1}{\pi z}\frac{4}{x}\frac{W}{pV}, \tag{1}$$

$$\tan(\beta-\theta) = \frac{2+(\gamma-1)\times M^2\sin^2\beta}{(\gamma+1)\times M^2\sin\beta\times\cos\beta} \approx \frac{1}{\sqrt{M^2-1}}, \tag{2}$$

where θ denotes the inclination angle of the virtual profile, β is the angle of discharge-induced shock wave; x and z represent the maximum length and thickness of the plasma virtual profile, respectively; M refers to the Mach number of the supersonic inflow, W is the mean discharge power, V is the mainstream velocity, and P is the static pressure. It should be noted that energy transformation ratio is not considered and W should be replaced by ηW.

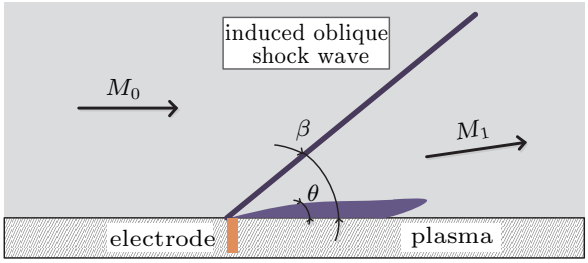


Fig. 11. Scheme of formation of induced oblique shock wave

To validate these equations, the variation of β with W is fitted by experimental data. As shown in Fig. 12, the theoretical fit is in good agreement with experimental data, suggesting that the loading power can significantly determine the control effect. The experimental data are sourced from schlieren images, as shown in Fig. 13. Table 3 shows the detailed values of various parameters in Eqs. (1) and (2). The schlieren images are obtained by performing mean gray processing on 4000 original images, thereby ensuring the accuracy of the experimental data.

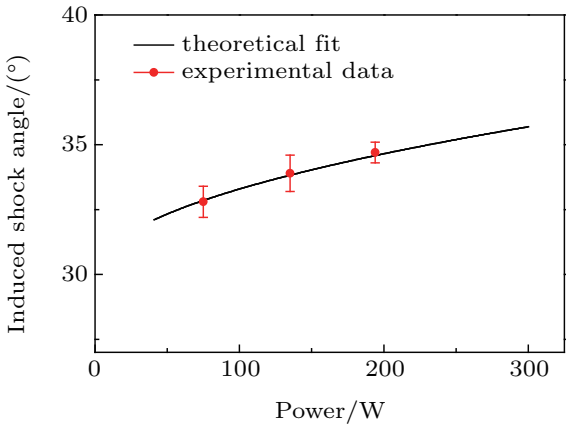


Fig. 12. Theoretical fit to experimental data of induced shock wave angle.

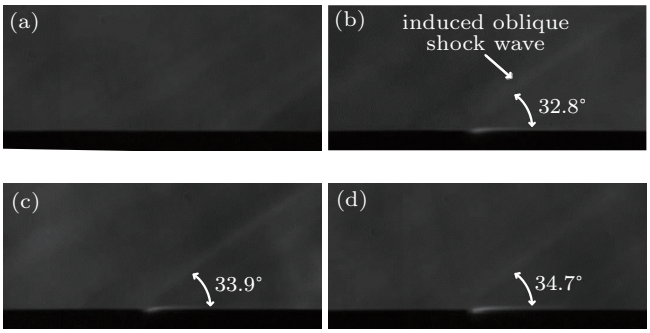


Fig. 13. Schlieren photos of the induced shock wave at (a) baseline, (b) 71 W, (c) 132 W, and (d) 196 W.

Table 3. Parameters for theoretical fit.

Parameters	P/kPa	x, z/mm	M	V/(m/s)	η
Value	12.218	10, 3	2	514	0.2

4.2. Experiments on controlling ramp-induced oblique shock wave under RF discharge plasma aerodynamic actuation

Figure 14 shows the evolution process of the ramp-induced oblique shock wave control under RF discharge plasma actuation. Since the compression ramp has a small inclination angle, the oblique shock wave almost exhibits no separation. At $\Delta T = 25$ μs, discharge-induced oblique shock wave with a height of H1 is observed at the bottom of ramp-induced oblique shock wave. However, the compression wave is not observed, suggesting that the compression wave imposes minor effect on the flow field. At $\Delta T = 50$ μs, discharge-induced shock wave further propagates to a height of H2, and the structure at the bottom of oblique shock wave begins to be scattered. Subsequently, from $\Delta T = 75$ μs to $\Delta T = 175$ μs, the discharge-induced oblique shock wave extends to a height of H3 and converges with the ramp-induced oblique shock wave. The boundary point of the scattered shock wave gradually elevates and is finally maintained at the same height. This change in ramp-induced shock wave structure is similar to the result demonstrated by Leonov *et al.*[24] and Falempin *et al.*[25]

For a better visualization of the change of ramp-induced shock wave structure, the spatial gradient calculations are conducted on the schlieren image, thereby extracting shock wave structure from the flow field. The spatial gradient of schlieren image can be extracted as follows:[26]

$$I_{xy} = \sqrt{\left(\frac{\partial I}{\partial x}\right)^2 + \left(\frac{\partial I}{\partial y}\right)^2}, \tag{3}$$

where I denotes the intensity of each pixel in the schlieren image (*i.e.*, the density gradient), and I_{xy} refers to the spatial gradient of the pixel intensity of the coordinate (x, y) in the schlieren image. Figure 15(b) shows the processed results on the datum flow field in Fig. 15(a), where the oblique shock wave is more evident. Since the airflow velocity is low at the bottom of the shock wave and around the wall, pixel intensities are unchanged and only sparse black points are observed at the corresponding positions. Additionally, no installation wave is observed in Fig. 15(b) since it is relatively weak.

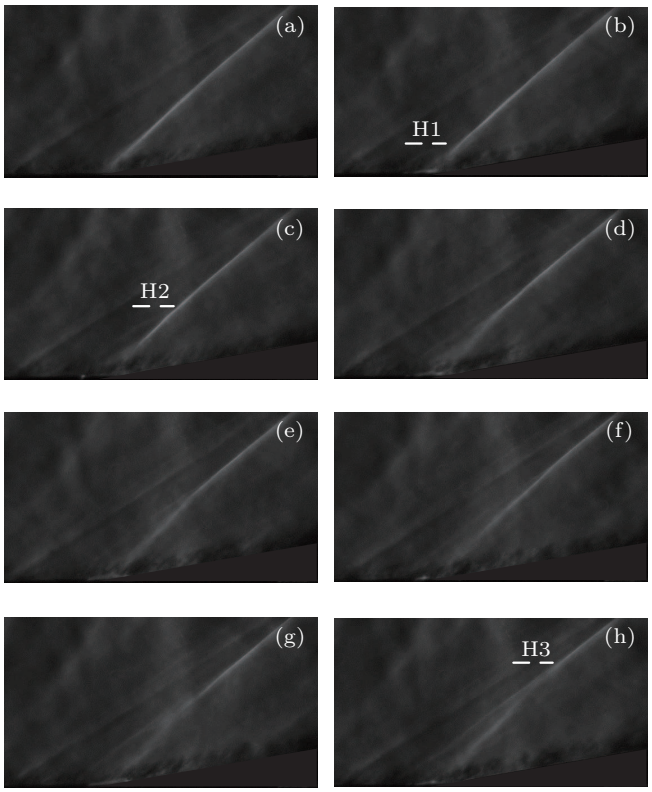


Fig. 14. Time-resolved schlieren visualization of the ramp-induced oblique shock wave control process with plasma actuation at (a) $\Delta T = 25$ μs, (b) $\Delta T = 50$ μs, (c) $\Delta T = 75$ μs, (d) $\Delta T = 100$ μs, (e) $\Delta T = 125$ μs, (f) $\Delta T = 150$ μs, (g) $\Delta T = 175$ μs, and (h) $\Delta T = 200$ μs.

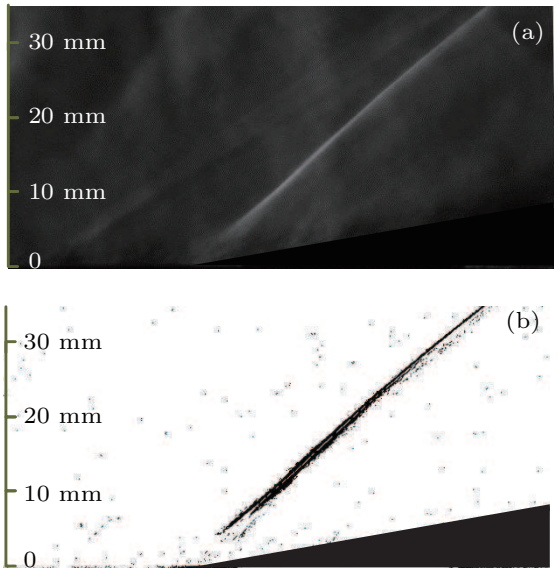


Fig. 15. Visualization of baseline flow field: (a) schlieren snapshot and (b) intensity gradient in the same schlieren image.

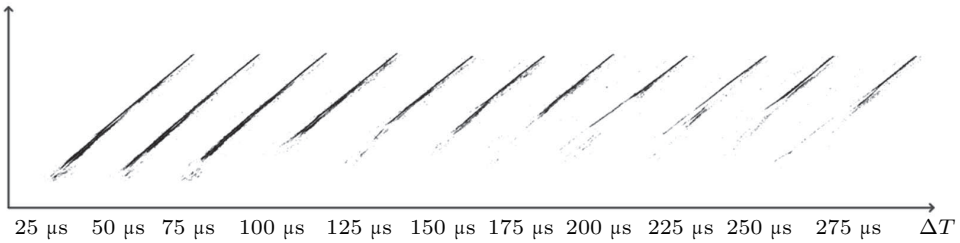


Fig. 16. Evolution process of oblique shock wave system under actuation.

Figure 16 shows the extracted shock wave structures at different time intervals according to the previously described method. From $\Delta T = 25$ μs to $\Delta T = 175$ μs, the discharge-induced scattered shock wave becomes more prominent as seen evidently from the black area at the bottom of oblique shock wave. Thus, it can be concluded that the gradient magnitude is weak. At $\Delta T = 200$ μs, the shock wave structure remains unchanged, indicating that the actuation control reaches a stable state.

4.3. Control principle of oblique shock wave under RF discharge plasma aerodynamic actuation

The experimental results of the shock wave control by surface arc actuation under the supersonic condition, given in previous studies are basically similar to the results obtained in this paper.[25] Therefore, surface arc discharge has certain reference significance for the research on the mechanism of RF actuation control shock wave.

According to the control mechanism of surface arc discharge, the dispersion of shock wave after the application of actuation is due to the fact that the discharge can rapidly heat the boundary layer and enhance gas turbulence.[13] In order to validate the change of boundary layer induced by RF discharge plasma aerodynamic actuation, in this study we use a correlation method for calculating the evolution of vortex cluster in the boundary layer[27,28]

$$C_{kl}(i,j) = \frac{1}{N_t}\sum_{n=1}^{N_t}\frac{[I_{ij}(n)-\bar{I}_{ij}][I_{kl}(n)-\bar{I}_{kl}]}{\sigma_{ij}\sigma_{kl}}, \tag{4}$$

where $I_{ij}(n)$ denotes the pixel intensity at the coordinate (i,j) in the n-th schlieren image, $I_{kl}(n)$ the pixel intensity at any a point (k,l) in the image; $\bar{I}_{ij}$ and $\bar{I}_{kl}$ represent the mean pixel intensities at the coordinates (i,j) and (k,l) in all images, respectively, σ_{ij} and σ_{kl} the standard deviations of pixel intensity at the coordinates (i,j) and (k,l) in all images, respectively. In order to use the correlation method, a reference point is selected in the shock wave or the boundary layer; then, the correlation with the surrounding flow field is investigated based on the pixel intensity, of which the result is unlike the wall pressure measurement.[27] In order to enhance the calculation precision, 5000 schlieren images with a resolution of 432×296 pixels are selected for processing; meanwhile, point P (266, 275) is set to be the reference point and the related correlation images are generated as shown in Fig. 17.

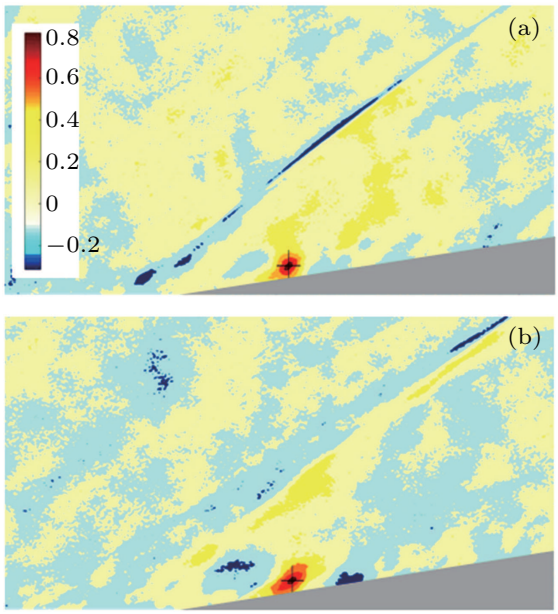


Fig. 17. Correlations when the reference point P (266, 275) (+symbol) is at the boundary layer (a) without and (b) with actuation.

By comparing these two images, it can be observed that after discharge the positive-correlation region around point P increases marginally, and negative-correlation regions adjacent to both upstream and downstream are also more apparent. This result is consistent with those of earlier studies where the negative-correlation region is observed near the positive-correlation region with the reference point upstream and downstream. In addition, the characteristic structure of the vortex cluster can be characterized by both magnitude and size.[15] Hence, it can be concluded that the vortex cluster in the boundary layer expands after the application of actuation.

Numerical simulations are performed for precisely analyzing the structure of shock wave boundary layer and different flow field parameters. The typical plate-ramp mesh model consists of 962644 cells, where the spacing ratio near wall is set to be 1.2 and the mesh height at the bottom is

10^{-5} m, thereby ensuring $y+ < 1$. The boundary conditions are identical to the experimental conditions as listed in Table 1. The calculation is based on the solutions of Reynolds-averaged, N–S equations with shear stress transport (SST) k–ω model. During the setting up of the heat source, the instantaneous power curve is smoothed to extract the change in power as shown in Fig. 18. Obviously, the simulation precision is enhanced compared with the sine waveforms by Wang *et al.*[18] A W-shaped single-cycle power curve is observed with a frequency of 1.3 MHz and a maximum power density of 5.9×10^{10} W/m^3.

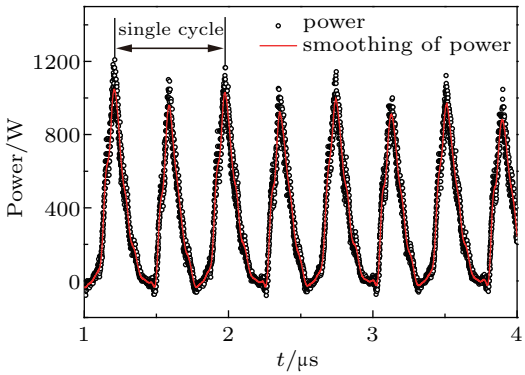


Fig. 18. Experimental instantaneous power waveforms and their simplified style for simulating the energy deposition of discharge.

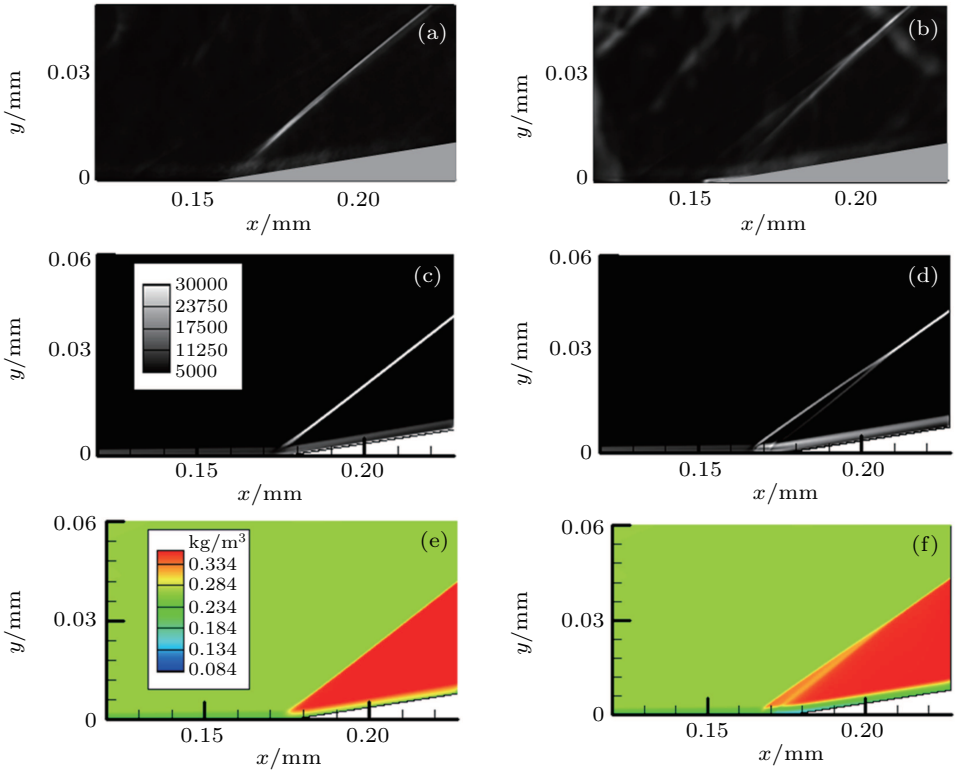


Fig. 19. RMS schlieren image (a) without and (b) with actuation. Density gradient image (c) without and (d) with actuation. Density image (e) without and (d) with actuation

To examine the accuracy of the experimental results and also for validating the reliability of the simulation results, root-mean-square (RMS) schlieren images are compared with density gradient images as shown in Fig. 19. Each RMS schlieren image is processed from 4000 schlieren images. From this comparison, it is evident that the shock wave structure in density gradient images is similar to that in the RMS schlieren images before and after the application of actuation. The boundary layer in the downstream of the actuation position is also significantly thickened after the application of actuation. This is equivalent to the coverage of a layer of low-density smooth wall on the ramp surface, thereby weakening the compressibility at the compression corner.[25] Moreover, the density of the boundary layer drops noticeably after the application of actuation and this confirms the previous analysis, as shown in Figs. 19(e) and 19(f).

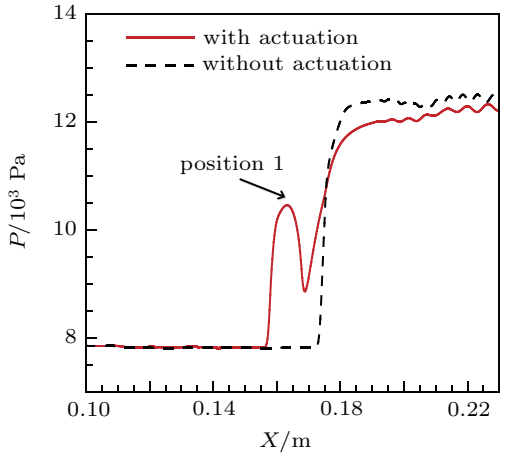


Fig. 20. Pressure variation along the wall surface with and without actuation.

Figure 20 shows the comparison between the distribution patterns of wall pressure before (black dashed line) and after (red solid line) the application of actuation. After discharge, the pressure at position 1 increases because of the decline in the local Mach number, whereas the pressure on the surface of the boundary layer behind the shock wave is lower than the baseline pressure without actuation. The present conclusions are consistent with the results demonstrated by Wang *et al.*[21]

5. Conclusions

We first performed wind tunnel experiments to investigate the characteristics of RF discharge plasma aerodynamic actuation and flow control. The control mechanism is then explored with the help of correlations and numerical simulations. Our main conclusions are described below.

Under the supersonic condition, diffuse discharge plasma mass is blown downstream. At the same time, the peak current drops while the peak voltage increases.

The RF discharge not only produces energy deposition on the electrode surface but also induces compression wave. The compression wave exhibits different propagation velocities under different operating pressures. At an operating pressure of 20 Torr, the velocity of the compression wave reaches a maximum value of 430 m/s, whereas a minimum velocity is observed at 60 Torr and 100 Torr. The energy deposition volume in RF surface discharge has a semicircular cross-section and gradually increases with time going by. In the energy deposition process, the maximum discharge temperature reaches up to 570 K.

Under the supersonic condition, the compression wave induced by RF discharge plasma is distorted under the action of airflow and an oblique shock wave is generated around the electrode. The stable oblique shock wave is obtained due to the continuous RF discharge. The RF discharge plasma scatters the structure on the bottom of the oblique shock wave, and this effect can also be steadily maintained.

The positive-correlation region corresponding to the reference point in the boundary layer increases marginally after the application of actuation, and the adjacent negative-correlation regions in both upstream and downstream also increase significantly. Accordingly, the vortex cluster in the boundary layer expands after the application of actuation. The boundary layer in the downstream of the actuation position density gradient images and RMS images are thickened noticeably, which is equivalent to the coverage of a layer of low-density smooth wall on the slope surface. Consequently, the compressibility at the compression corner is weakened. It can be observed from the density cloud charts that the density in the boundary layer after the application of actuation drops significantly, which also confirms the previous analysis. The variation of wall pressure reveals that the discharge can reduce the local Mach number and increase the pressure. The pressure on the surface of boundary layer behind the wave is lower than the datum pressure after application of actuation.

References

[1] Wu Y and Li Y H 2015 *Acta Aeronautica ET Astronautica Sinica* **36** 381
[2] Russell A, Zare-Behtash H and Kontis K 2016 *J. Electrostat.* **80** 34
[3] Menart J, Shang J, Atzbach C, Magoteaux S, Slagel M and Bilheimer B 2005 43*rd AIAA Aerospace Sciences Meeting Exhibit*, January 10–13 2005, Reno, USA, p. 947
[4] Azarova O A and Knight D D 2015 *Aerosp. Sci. Technol.* **43** 343
[5] Yan H, Liu F, Xu J and Xue Y 2018 *AIAA J.* **56** 1
[6] Wang H Y, Li J, Jin D, Dai H, Gan T and Wu Y 2017 *Chin. J. Aeronaut.* **30** 1854
[7] Leonov S and Yarantsev D 2008 *Fluid Dyn.* **43** 945
[8] Menier E, Leger L and Depussay E 2007 *J. Phys. D: Appl. Phys.* **40** 695
[9] Joussot R, Lago V and Parisse J D 2015 *Exp. Fluids* **56** 102
[10] Jin D, Cui W, Li Y H, Li F Y, Jia M, Sun Q and Zhang B L 2015 *Chin. J. Aeronaut.* **28** 66
[11] Nishihara M, Gaitonde D and Adamovich I V 2013 51*st AIAA Aerospace Sciences Meeting Including New Horizons Forum Aerospace Exposition*, January 7–10, 2013, Grapevine, USA, p. 461
[12] Nishihara M, Takashima K, Rich J W and Adamovich I V 1980 *Phys. Fluids* **23** 605
[13] Lashkov V, Mashek I, Anisimov Y, Ivanov V, Kolesnichenko Y and Ryvkin M 2004 42*nd AIAA Aerospace Sciences Meeting Exhibit*, January 5–8, 2004, Reno, USA, p. 671
[14] Wang H Y, Li J, Jin D, Zhang Z B, Tang M X and Wu Y 2017 *Int. J. Heat Fluid Flow* **67** 133
[15] Klimov A, Grigorenko A and Efimov A 2014 52*nd Aerospace Sciences Meeting*, January 13–17, 2014, National Harbor, USA, p. 0960
[16] Dedrick J, Im S and Cappelli M A 2013 *J. Phys. D: Appl. Phys.* **46** 405201
[17] Wang W L, Li J and Song H M 2017 *Chin. Phys. B* **26** 015205
[18] Wang W L, Song H M, Li J, Jin D, Jia M and Wu Y 2017 21*st AIAA International Space Planes Hypersonics Technologies Conference*, March 6–9, 2017, Xiamen, China, p. 2283
[19] Wang J, Li Y H and Cheng B Q 2009 *J. Phys. D: Appl. Phys.* **42** 165503
[20] Wang J, Li Y H and Xing F 2009 *J. Appl. Phys.* **106** 073307
[21] Jin D, Li Y H and Jia M 2014 *Chin. Phys. B* **23** 035201
[22] Yang Z, Song H M, Wang H Y, Guo S G, Jia M and Wang K 2018 *Chin. Phys. B* **27** 378
[23] Leonov S and Yarantsev D 2008 *J. Propul. Power* **24** 1168
[24] Leonov S, Firsov A, Yarantsev D, Falempin F and Goldfeld M 2013 17*th AIAA Interational Space Planes & Hypersonic Systems & Technologies Conference*, April 11–14, 2011, San Francisco, USA, p. 2362
[25] Falempin F, Firsov A, Yarantsev D, Goldfeld M, Timofeev K and Leonov S 2015 *Exp. Fluids* **56** 1
[26] Gan T, Wu Y, Sun Z Z, Jin D, Song H M, Jia and M 2018 *Phys. Fluids* **30** 055107
[27] Sartor F, Mettot C, Bur R and Sipp D 2015 *J. Fluid Mech.* **781** 550
[28] Dupont P, Haddad C and Debiève J F 2006 *J. Fluid Mech.* **559** 255